Lockett, R. D., Jeshani, M., Makri, K. & Price, R. (2016). An Optical Characterization of Atomization in Non-Evaporating Diesel Sprays. SAE Technical Papers, 2016-01-0865. doi: 10.4271/2016-01-0865

An Optical Characterization of Atomization in Non-Evaporating Diesel Sprays

[1]R.D. Lockett, [1]M. Jeshani, [1]K. Makri, [2]R. Price

[1]Department of Mechanical Engineering & Aeronautics, City University, London.

[2]Shell Global Solutions, Brabazon House, Manchester

Abstract

High-speed planar laser Mie scattering and Laser Induced Fluorescence (PLIF) was employed for the determination of Sauter Mean Diameter (SMD) distribution in non-evaporating diesel sprays. The effect of rail pressure, distillation profile, and consequent fuel viscosity on the drop size distribution developing during primary and secondary atomization was investigated.

Samples of conventional crude-oil derived middle-distillate diesel and light distillate kerosene were delivered into an optically accessible mini-sac injector, using a customized high-pressure common rail diesel fuel injection system. Two optical channels were employed to capture images of elastic Mie and inelastic LIF scattering simultaneously on a high-speed video camera at 10 kHz.

Results are presented for sprays obtained at maximum needle lift during the injection. These reveal that the emergent sprays exhibit axial asymmetry and vorticity. An increase in the rail pressure was observed to lead to finer atomization, with larger droplets observable in the neighbourhood of the central axis of the spray, decreasing with radius towards the spray boundaries. Finally, the light kerosene was observed to produce smaller droplets (as measured by Sauter mean diameter), relative to the conventional diesel, suggesting a correlation between distillation profile and viscosity, and mean spray droplet size.

Introduction

Combustion efficiency, thermal efficiency and engine-out emissions are strongly dependent on the characteristics of the diesel sprays that are formed in modern direct injection common rail diesel engines [1]. A careful examination of the atomization of diesel sprays is essential therefore, in order to obtain a suitable optimization of the parameters that are capable of producing an improvement in the pre-combustion fuel-air mixing, in order to obtain the reduced engine-out emissions required by national/inter-national regulations.

The combustion occurring in the engine cylinders from a diesel spray originates from a number of auto-ignition sites forming around the spray head, which then spread rapidly along the fuel vapour-air mixture surrounding the atomized spray head, finally resulting in regions of turbulent partially-premixed and non-premixed flames [2]. Diesel combustion is naturally rate-controlled by the sequential rates of liquid breakup (atomization), evaporation, flow and/or diffusional mixing, auto-ignition and flame spread [3]. In most diesel engines, the atomized diesel spray originates from a multi-hole diesel injector nozzle, which enables the high velocity propulsion of the liquid fuel into the cylinder volume. A high pressure pump is employed to

maintain the fuel at high pressure in a pressure accumulator (common rail), and inside the injector bodies. An injector needle connected to an electronic activation system is employed to seal the injector body and upper nozzle passages from the lower nozzle exit holes when the injector is inactive, and to expose the lower tip of the nozzle and the exit holes to the high pressure liquid fuel when the injector is electronically activated. This exposure causes the high pressure fuel to flow down the fuel passage into the tip of the nozzle, through the nozzle holes, and into the engine cylinder volume.

It is believed that the fuel flow occurring in the nozzle holes during diesel fuel injection is a multi-phase cavitation flow. This has been observed and reported in a number of model investigations, which have identified two distinct types of cavitation occurring in the nozzle holes: (1) sheet (geometric) cavitation occurring at the upper entrance of the nozzle holes [4 – 7], and (2) vortex flow cavitation occurring along the central axis of the nozzle holes [6 – 8].

The cavitation flow occurring in the nozzle holes will affect the structure of the liquid leaving the holes and entering the engine cylinder during fuel injection. This will in turn affect the interaction of the liquid jets leaving the nozzle holes with the cylinder air. The breakup of the liquid jets to eventually form travelling droplets is generally considered to occur in two stages; primary breakup followed by secondary breakup [9 - 11].

Faeth et al. [11] have undertaken an extensive review of work relating to the structure of sprays and the spray breakup mechanisms. The following is a summary of their review. They suggest that primary breakup of the liquid jet occurs when the turbulent bulk liquid leaves the nozzle holes and enters the surrounding air. The sudden change in boundary conditions and pressure distribution enables increased shear, radial flow acceleration and the development of surface instabilities due to liquid flow turbulence. The emitted liquid also encounters the surrounding gas, which may itself be subject to stochastic, bulk movement (turbulence). The local drag forces exerted by the surrounding gas on the moving sections of turbulent liquid are able to contribute to the growth of the surface instabilities which lead to primary breakup. This process is named aerodynamically assisted primary breakup, and is likely to be the dominant mechanism for primary breakup of diesel sprays in diesel engines.

The combination of turbulence and aerodynamic drag destabilizes the liquid surface by overcoming the internal stabilizing forces of surface tension and viscosity. The continuum liquid surfaces begin to distort, forming large-scale surface waves [12]. As the liquid travels further in the surrounding gas, the liquid turbulence and local aerodynamic drag cause the surface waves on the surface of the bulk liquid to grow and deepen, eventually leading to surface break-down and liquid separation. This results in the formation of unstable liquid tubes (ligaments) and large, unstable, oscillating liquid drops surrounding a dense liquid core. Wu et al. [13] and Wu and Faeth [14] developed a phenomenological model for the distance x_i from the nozzle exit where turbulent primary breakup begins, which is expressed as

$$x_i/\Lambda = C_{xt}(\bar{u}_0/v'_{rms})^{9/5} We_{L\Lambda}^{-0.4} \qquad (1)$$

where Λ, $\bar{u}_0$, v'_{rms} and $We_{L\Lambda}$ are the integral length scale of the liquid jet turbulence, the mean axial velocity, the root-mean-square radial component of turbulent velocity fluctuation, and the Weber number for the jet respectively. ($We_{L\Lambda} = \rho_l \Lambda \bar{u}_0^2/\sigma$, where ρ_l is the liquid state density and σ is the surface tension of the liquid.) Available data has been employed to derive an empirical equation for x_i, which is expressed as

$$x_i/\Lambda = 3890 We_{L\Lambda}^{-0.67}. \qquad (2)$$

As the liquid from the jet is propelled further into the surrounding gas, primary breakup occurring at the surface of the liquid core reduces the net continuum liquid volume comprising the core. Cheroudi et al. [15] have estimated the nozzle diameter (d) normalized distance the liquid core survives primary atomization (l_c) to be

$$l_c/d = C_c\left(\rho_l/\rho_g\right)^{1/2} \tag{3}$$

where ρ_g is the vapor state density, and C_c is an empirical constant in the range of 7 – 16. The local Sauter mean diameter d_{32} (mean droplet diameter corresponding to the local volume to surface area ratio) of liquid elements (droplets and ligaments) produced by primary breakup is represented reasonably well by the empirical expression

$$d_{32} = 0.65\Lambda\left(x/\Lambda We_{L\Lambda}^{1/2}\right)^{2/3}. \tag{4}$$

The region surrounding the liquid core of the jet is filled with large droplets and ligaments. Secondary breakup is the process by which aerodynamic forces (normally drag) cause the large droplets and ligaments formed during primary breakup to break up into smaller droplets. This process continues until the remaining droplets in the fully atomized spray are of a size distribution such that the droplets are stable to the aerodynamic forces exerted on them by the surrounding gas [11, 12]. A phenomenological analysis of secondary atomization, combined with empirical data fitting [16] has led to an estimate for the dominant Sauter mean diameter for droplets resulting from secondary atomization. This is

$$d_{32} = \frac{6.2\sigma}{\rho_g u_0^2}\left(\rho_l/\rho_g\right)^{1/4} We.Re_{Ld}^{-1/2} \tag{5}$$

where Re_{Ld} is the liquid jet Reynolds number ($Re_{Ld} = \rho_l u_0 d/\mu_l$).

For conditions where aerodynamic forces are important (atomization in a diesel engine), primary breakup and secondary breakup merge with increasing distance downstream of the nozzle exit. A best fit correlation of Sauter mean diameter for droplets formed as a result of merged primary and secondary breakup can be expressed as

$$d_{32} = \frac{12.9\sigma}{\rho_g u_0^2}(x/\Lambda)^{1/3}\left(\rho_l/\rho_g\right)^{3/2} We_{L\Lambda}^{5/6}.Re_{L\Lambda}^{-1/2}. \tag{6}$$

Ghuri et al. [17], Jankowski et al. [18], and Chen et al. [19] investigated the effect of injection pressure and fuel type on various spray characteristics such as penetration length, spray cone angle, and droplet size distribution. In particular, they observed that high viscosity fuels produced longer penetration length and bigger droplet sizes. This was attributed to the relatively larger cohesive forces which resulted in higher resistance to break-up and thus bigger droplets. Subsequently, the large droplets of high spray momentum were able to penetrate further into the ambient gas. They also concluded that the injection pressure affected the size of the droplets; higher injection pressures resulted in smaller droplets being produced, due to the increase of turbulent flow drag exerted on the larger droplets by the surrounding gas flow.

The primary objective of the present work was the identification of the dependence of spray structure and droplet size distribution developing during primary and secondary atomization on diesel fuel properties (distillation profile, viscosity, density and surface tension). In this regard, it was possible to investigate these effects in idealized, non-evaporating sprays obtained from a customized diesel fuel injection equipment (FIE) system at moderate injection

pressures. The present work therefore focuses on secondary atomization in diesel sprays obtained from 250 bar and 350 bar rail pressures respectively, in order to identify the effect of distillation profile, viscosity, surface tension and rail pressure on the drop size distribution and the structure of the emerging sprays. Quantitative measurements may also be employed for comparison with phenomenological model and CFD model prediction, and in the calibration of CDF models.

Diagnostics that are suitable for an experimental investigation into primary and secondary atomization in idealized diesel sprays include phase Doppler anemometry (PDA) [20], laser Mie scattering [21], laser induced fluorescence (LIF) [22], laser sheet dropsizing (LSD, combined LIF/Mie scattering) [23 - 25], structured illumination planar laser imaging (SLIPI, an extension of LSD) [26], ballistic imaging [27], and ultra-small angle x-ray scattering (USAXS) [28].

Phase Doppler anemometry is a point-wise measurement technique that is capable of the determination of mean spherical droplet size and velocity in a localized region of a spray. It has been employed successfully in many spray applications and has proved useful in the analysis of a range of dilute sprays, including in the diluted region of gasoline and diesel sprays. However, the technique is unable to produce reliable data in dense sprays due to optical attenuation, and in sprays where the liquid has broken up into ligaments and/or elliptical droplets.

Laser Mie scattering is a useful qualitative technique widely used to identify and characterize the qualitative structure of a spray. It has been employed as a quantitative tool in the determination of spray cone angle, spray head displacement and velocity as a function of injection rate, needle lift, upstream liquid pressure, and downstream gas pressure and temperature. In the limiting case of the droplet mean diameter d being very much larger than the wavelength λ of the scattering light ($d >> \lambda$), the scattering is proportional to the total surface area of the local field of droplets. As a result it is difficult to extract useful quantitative data about the spray atomization process from the scattered light.

Laser induced fluorescence is a useful, quantitative technique that is capable of capturing single-shot two-dimensional planar field information from a spray. The technique relies on the photographic capture of fluorescence emission from optically excited molecules in solution in the spray medium. The intensity of the optical emission is dependent on the local spectral flux density, the concentration of the fluorescent component in solution, and the amount of optical saturation occurring. The fluorescence emission is volumetric, thereby capable of providing a quantitative measurement of local liquid volume fraction. It is capable of similar measurements to Laser Mie scattering. In addition, it is capable of providing detailed quantitative measurements on the structure of sprays, through the measurement of local liquid volume fraction. However, the optical excitation and emission is difficult to calibrate in optically dense (turbid) media subject to significant optical attenuation, and it is subject to defocusing effects when multiple scattering is present. Evaporating sprays require a co-evaporative fluorescent marker molecule in solution in order to maintain a self-consistent fluorescence yield from the evaporating droplets. Failure to achieve this results in biased fluorescence yield.

Laser sheet drop-sizing combines the benefits of laser Mie scattering and laser induced fluorescence in order to provide quantitative two-dimensional information on the structure of sprays. The precise spatial ratio of the local LIF signal intensity with the local Mie signal intensity provides a two-dimensional spray field measurement of droplet Sauter mean diameter

d_{32}. The accuracy of the technique is dependent on the fluorescence emission being volumetric, and the ability to calibrate for the spatial variation in excitation laser spectral flux density. The technique is limited to low turbidity sprays (sprays satisfying line-of-sight optical transmission factor $T \geq 1/e$). This criterion ensures that defocusing effects due to multiple scattering are small, and can be neglected.

Structured illumination planar laser imaging is an extension of laser sheet drop-sizing, which provides an in-situ method for calibrating out the defocusing effect of multiple scattering from a turbid medium (an optically dense spray, for example). While it offers an improvement to the resolution achievable in laser sheet drop-sizing (by reducing the defocusing associated with multiple scattering), it is difficult to implement in a real application.

Ballistic imaging is an optical technique that involves separating out photons traversing a turbid medium on a temporal basis. Time-resolved capture of photons traversing the turbid medium without scattering provides the opportunity to identify optical paths of varying absorption through the medium. This enables the identification of dense flow structures (the spatially varying structure of the spray core) within an optically dense spray. The technique is based on line-of-sight transmission and scattering, thereby averaging features over line-of-sight. However, this limitation can be addressed by a tomographic methodology, combined with tomographic reconstruction.

The Mechanical Engineering laboratories at City University have the capability to utilize phase Doppler anemometry, laser Mie scattering, laser induced fluorescence, laser sheet drop-sizing, and structured illumination planar laser imaging. Laser sheet drop-sizing was selected as the most appropriate diagnostic in terms of capability and experimental complexity in the context of the idealized low turbidity, non-evaporative diesel sprays to be investigated.

Background to Laser Sheet Drop-Sizing (LSD)

Laser Sheet Drop-sizing (LSD) is a recently developed laser diagnostic which combines Planar Laser Induced Fluorescence with Planar Lorentz-Mie Scattering in a spray in order to obtain instantaneous full-field measurements of Sauter Mean Diameter (spray droplet volume to surface area ratio) and liquid volume fraction. The technique was originally developed by Kamimoto et al. [23], and more recently developed at Cranfield University by Le Gal et al. [24] and Jermy and Greenhalgh [25], and applied to diesel sprays by Lockett et al. [29, 30]. The technique has been investigated and developed further by Domann and Hardalupas [31].

The LSD technique is based on the notion that laser induced fluorescence (LIF) obtained locally from a field of droplets containing a fluorescent agent is volumetric, while elastic Mie scattering obtained from a field of droplets is proportional to surface area (conditional on droplet diameter d being very much larger than the scattering wavelength λ). The ratio of the two optical signals obtained from a spray should provide an instantaneous two-dimensional field measurement of spray volume to surface area ratio (Sauter mean diameter d_{32}).

The far-field Lorentz-Mie scattering cross-section for large, homogeneous, weakly absorbing dielectric spherical scatterers resorts to the corresponding results obtained from geometrical optics [32, 33]. The contributions to the differential scattering cross-section in the geometrical optics limit are from Fraunhofer diffraction, specular reflection, refraction, and external scattering arising from internal reflections. The particle size scattering parameter β is defined

to be $\boldsymbol{\beta = \pi d/\lambda}$, where d is the diameter of the scattering sphere and λ the scattering wavelength. The far-field Lorentz-Mie scattering cross-section may be thought of in terms of the sum of scattered partial waves [33]. The scattered light is expressed in terms of the scattering amplitude matrix

$$\begin{pmatrix} \boldsymbol{E_2} \\ \boldsymbol{E_1} \end{pmatrix}_{\boldsymbol{sc}} = \frac{\boldsymbol{e^{ikr}}}{\boldsymbol{ikr}} \begin{pmatrix} \boldsymbol{S_2} & \boldsymbol{0} \\ \boldsymbol{0} & \boldsymbol{S_1} \end{pmatrix} \begin{pmatrix} \boldsymbol{E_2} \\ \boldsymbol{E_1} \end{pmatrix}_{\boldsymbol{in}} \tag{7}$$

where E_{isc}, S_i and E_{iin} are the scattered electric field strength, the scattering amplitude, and the incoming electric field strength for the i'th polarization respectively.

The far-field Lorentz-Mie scattered electric fields are expressed as

$$\boldsymbol{E_\varphi = iE_0 sin\varphi \frac{e^{iK_0 r}}{K_0 r} \sum_{l=1}^{\infty} \frac{2l+1}{l(l+1)} \left(a_l \frac{P_l^1(cos\theta)}{sin\theta} + b_l \frac{dP_l^1(cos\theta)}{d\theta} \right)} \tag{8}$$

$$\boldsymbol{E_\theta = -iE_0 cos\varphi \frac{e^{iK_0 r}}{K_0 r} \sum_{l=1}^{\infty} \frac{2l+1}{l(l+1)} \left(a_l \frac{dP_l^1(cos\theta)}{d\theta} + b_l \frac{P_l^1(cos\theta)}{sin\theta} \right)}, \tag{9}$$

where $\boldsymbol{K_0 = kn}$ (n is the relative refractive index of the scattering sphere).

The Lorentz-Mie differential scattering cross-section can be expressed as

$$\boldsymbol{\frac{d\sigma}{d\Omega} = \frac{1}{k^2} (|S_2|^2 cos^2\varphi + |S_1|^2 sin^2\varphi)} \tag{10}$$

where

$$\boldsymbol{S_1(\beta,\theta) = \sum_{l=1}^{\infty} \frac{2l+1}{l(l+1)} \left(a_l \frac{P_l^1(cos\theta)}{sin\theta} + b_l \frac{dP_l^1(cos\theta)}{d\theta} \right)} \tag{11}$$

$$\boldsymbol{S_2(\beta,\theta) = \sum_{l=1}^{\infty} \frac{2l+1}{l(l+1)} \left(a_l \frac{dP_l^1(cos\theta)}{d\theta} + b_l \frac{P_l^1(cos\theta)}{sin\theta} \right)}. \tag{12}$$

The l'th partial wave scattering coefficients $\boldsymbol{a_l}$ and $\boldsymbol{b_l}$ may be expressed as

$$\boldsymbol{a_l(\beta) = \frac{\psi_l(\beta)\psi_l'(n\beta) - n\psi_l(n\beta)\psi_l'(\beta)}{\zeta_l^{(1)}(\beta)\psi'_l(n\beta) - n\psi_l(n\beta)\zeta_l^{(1)'}(\beta)}} \tag{13}$$

$$\boldsymbol{b_l(\beta) = \frac{\psi_l(n\beta)\psi_l'(\beta) - n\psi_l'(n\beta)\psi_l(\beta)}{\zeta_l^{(1)'}(\beta)\psi_l(n\beta) - n\zeta_l^{(1)}(\beta)\psi_l'(n\beta)}}. \tag{14}$$

where $\boldsymbol{\psi_l(\beta) = \beta j_l(\beta)}$ and $\boldsymbol{\zeta_l^{(1)}(\beta) = \beta h_l^{(1)}(\beta)}$. $\boldsymbol{j_l(\beta)}$ and $\boldsymbol{h_l^{(1)}(\beta)}$ are the spherical Bessel function and spherical Hankel function respectively.

The total absorption cross-section σ_{abs} and scattering cross-section σ_{sc} from a scattering sphere are obtained by integrating the absorbed incident flux and the scattered flux over 4π solid angle

respectively. The sum of the absorption cross section σ_{abs} and the scattering cross-section σ_{sc} defines the total extinction cross-section σ_{ext} ($\sigma_{ext} = \sigma_{abs} + \sigma_{sc}$).

The scattering efficiency Q is defined relative to the geometric cross-sectional area of the scattering spheres, i.e

$$\boldsymbol{Q_{abs} = 4\sigma_{abs}/\pi d^2}\,, \boldsymbol{Q_{sc} = 4\sigma_{sc}/\pi d^2}. \quad (15)$$

In the geometrical optics limit of $\boldsymbol{\beta \to \infty}$ ($\boldsymbol{d \gg \lambda}$), $\boldsymbol{Q_{abs}}$ and $\boldsymbol{Q_{sc}}$ may be approximated (Debye approximation [33]) to be

$$\boldsymbol{Q_{abs}^{(go)} \approx 1 - \int_0^{\pi/2}(R_1 + R_2)cos\theta sin\theta d\theta} \quad (16)$$

and

$$\boldsymbol{Q_{sc}^{(go)} \approx 1 + \int_0^{\pi/2}(R_1 + R_2)cos\theta sin\theta d\theta}, \quad (17)$$

where R_1 and R_2 are the polarization-dependent reflectivities of the scattering spheres. Equation (17) shows that the scattering cross-section for weakly absorbing large spherical scatterers is proportional to the surface area of the scatterer ($\boldsymbol{\sigma_{sc} \propto d^2}$).

The optical absorption that occurs to the light incident on one or many scattering spheres may be due to the addition of a fluorescent agent to the scattering medium. Applying a two-level

fluorescence model that includes collision quenching, results in the governing equations for the molecular ground state (N_g) and excited state populations (N_e).

$$\frac{dN_g}{dt} = \left(A_{eg} + Q_{eg} + u_\omega B_{eg}\right)N_e - u_\omega B_{ge} N_g \tag{18}$$

$$\frac{dN_e}{dt} = -\left(A_{eg} + Q_{eg} + u_\omega B_{eg}\right)N_e + u_\omega B_{ge} N_g \tag{19}$$

subject to the total number of molecules $N = N_g + N_e$. u_ω, A_{eg}, B_{ge} and B_{eg} are the local spectral energy density of the laser radiation, the Einstein coefficient for spontaneous emission

(fluorescence), and the Einstein coefficients for stimulated absorption and emission respectively. Equation (19) becomes

$$\frac{dN_e}{dt} = -\left(A_{eg} + Q_{eg} + u_\omega B_{eg}\right)N_e + u_\omega B_{ge}(N - N_e). \tag{20}$$

During the passage of the laser through the fluorescence medium, the steady-state excitation and decay results in the saturation condition $dN_e/dt = 0$. Hence the steady-state ratio of excited state fluorescent molecules to the number of ground state fluorescent molecules is

$$\frac{N_e}{N_g} = \frac{u_\omega B_{ge}}{u_\omega B_{eg} + A_{eg} + Q_{eg}}. \tag{21}$$

Following the excitation laser pulse, the excited state population decays according to

$$N_e(t) = N_{e0}\exp\left(-\left(A_{eg} + Q_{eg}\right)t\right). \tag{22}$$

The fluorescence energy transmitted into an element of solid angle $\Delta\Omega$ in a time T is given by

$$\Delta E_{LIF} = \int_0^T \frac{N_e(t) A_{eg} \hbar\omega \Delta\Omega}{4\pi}\, dt \approx \frac{u_\omega B_{ge} \Gamma C \Delta V A_{eg} \hbar\omega \Delta\Omega \tau}{4\pi\left(u_\omega\left(B_{ge} + B_{eg}\right) + A_{eg} + Q_{eg}\right)}, \tag{23}$$

where Γ, $\hbar$, C, ΔV, and τ are a linewidth integral defining the overlap of the laser band-width with the absorption band line-width, Planck's angular momentum constant, the concentration of fluorescent agent in the scattering spheres, the volume that the laser traverses, and the duration of the laser respectively. Equation (23) shows that the local fluorescence yield is proportional to the number of fluorescent molecules present in the scattering target. This is, in turn, proportional to the volume of the target containing fluorescent molecules.

Le Gal et al. [24] utilized a droplet generator to demonstrate the d^2 dependence of the Lorentz-Mie scattering cross-section from droplets in the 20 µm to 100 µm range of sizes, and the d^n dependence of the laser induced fluorescence signal on fluorescent marker concentration. They

showed that the fluorescence is volumetric (d^3 dependence) for a range of fluorescent marker concentrations.

In a diffuse spray containing droplets, these relationships are expressed mathematically in the form

$$\Delta \boldsymbol{I_{LIF}} \propto \sum_{i=1}^{N} \boldsymbol{d_i^3}, \tag{24}$$

and

$$\Delta \boldsymbol{I_{Mie}} \propto \sum_{i=1}^{N} \boldsymbol{d_i^2}, \tag{25}$$

which has the consequence that

$$\frac{\Delta \boldsymbol{I_{LIF}}}{\Delta \boldsymbol{I_{Mie}}} \propto \frac{\sum_{i=1}^{N} \boldsymbol{d_i^3}}{\sum_{i=1}^{N} \boldsymbol{d_i^2}} \propto \boldsymbol{d_{32}}, \tag{26}$$

where ΔI_{LIF}, ΔI_{Mie} and d_i are the measured LIF and Mie scattering optical signals, and the diameter of the i'th droplet in the spray respectively.

Le Gal et al. [24] and Domann and Hardalupas [31] showed that the LIF signal is dependent on the concentration of the fluorescent marker in order to obtain an accurate volumetric measurement from the spray. In this case, the concentration of Rhodamine-B in the diesel is low, producing an extinction coefficient of approximately 0.25 cm^{-1}. Therefore the fluorescence emission obtained from the spray is likely to be volumetric.

Le Gal et al. [24] compared laser sheet drop-sizing measurements with phase Doppler anemometry measurements obtained from a swirl pressure atomizer. The LSD measurements were in good agreement with the PDA measurements, with a standard deviation to mean diameter ratio of 0.07. They conducted the measurements using a Pegasus Nd:YAG laser with a shot-to-shot standard deviation to mean pulse energy ratio of approximately 0.05 to 0.06. This suggests that much of the standard deviation achieved in the LSD measurements was due to the variation in shot-to-shot laser pulse energy, and that the precision attainable using LSD is principally determined by the stability of the exciting laser.

Berrocal et al. [26] have estimated the upper limit of precision of the LSD technique as a function of the optical density of the spray and defocusing effects due to multiple scattering. They concluded that the LSD technique is capable of retaining the precision identified by Le Gal et al. [24] as long as the attenuation coefficient T through the spray remained larger than 1/e (negligible secondary scattering). The model diesel sprays investigated in this study had relatively low optical density, and satisfied this criterion.

Experimental

Fuel Injection system

The high pressure fuel injection rig shown in Figure 1 was custom manufactured at City University and was able to generate common rail pressures of up to 700 bar. It was capable of introducing a precise quantity of fuel into the injector at a predetermined rate. The fuel was delivered from the tank to the high pressure diesel pump via a rotary vane priming pump and

a 5µm polypropylene filter. The diesel pump compressed the fuel and delivered it to a pressure accumulator (common rail), which was in turn, connected to a mini-sac diesel injector.

An automotive injector manufacturer provided a number of mini-sac diesel injector bodies and nozzles. Two of the injectors provided had been fitted with induction sensors in order to measure the needle lift. Figure 2 shows the 4.0 ms TTL pulse provided to the injector driver and the corresponding needle lift profile measured by the induction sensor at 400 bar common rail pressure.

The needle lift had an approximately constant lift rate of 0.10 mm/ms for approximately 3.0 ms, followed by a 0.3 ms duration, during which the needle achieved its maximum lift, followed by a 1.6 ms duration for needle return. The needle returned to its sealed position approximately 6.0 ms after the electronic start-of-injection signal. The needle lift was achieved using the same electronic driver unit as reported in Lockett et al. [8], in order to provide the injector with the same lift profile. This needle lift profile corresponds to moderate common rail pressures, and is typical for engines operating at idle or low/part load.

The electronic control box controlling the timing, duration and repetition rate of the fuel injection process provided a signal which was locked to the phase of the diesel pump, in order to achieve a stable and repeatable fuel pressure during injection. This was measured at the entrance port to the injector during the fuel discharge, using a Kulite ETMER-1-375M-3500BARSG pressure transducer. The transducer had a rated pressure of 3,500 bar SG (sealed gauge), and its sensitivity and zero balance were 1.189 mV/bar and 500 mV ± 50 mV respectively.

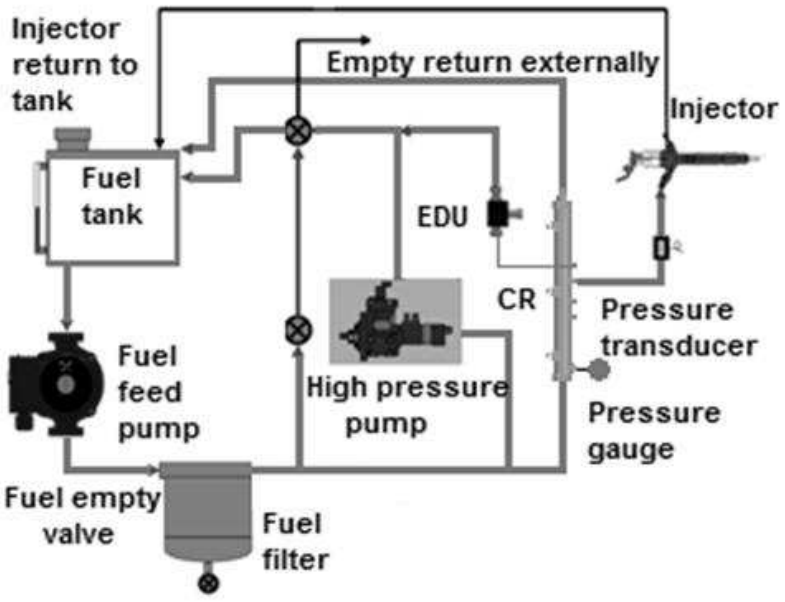

Figure 1: Schematic of fuel injection system.

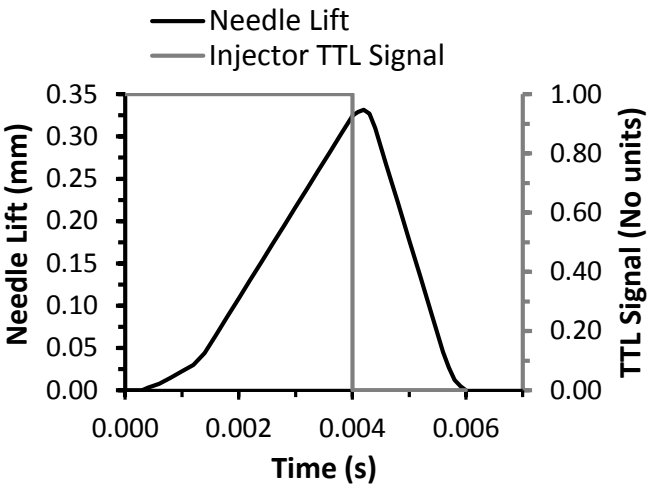

Figure 2: Mini-sac Diesel Injector Needle Lift Profile as a Function of TTL Signal.

A conventional injector was employed to measure the injected mass using the unadditized diesel sample A at 350 bar common rail pressure. A container of known mass was placed over the injector in order to capture the injected fuel. Five sets of 100 injections each were undertaken. The mass of the container and captured fuel was measured, facilitating the determination of the injected fuel mass. Over the course of five injection tests, the maximum and minimum injected fuel masses were measured to be 7.022 g and 7.017 g respectively. This means that the mean injected fuel mass per injection was 70.19 mg ± 0.02 mg. Given a nozzle hole Bernoulli velocity of 288.7 m/s (corresponding to 350 bar rail pressure), the measured injected mass corresponds to a discharge coefficient of approximately 0.830 based on a 4.0 ms injection period.

Injector design, tip holding mechanism

A conventional mini-sac diesel injector consisting of the injector body and 136 µm diameter six-hole mini-sac nozzle was employed in these experiments. The steel nozzle tip was removed from the base of the nozzle, and the mini-sac and six-hole nozzle tip replicated in clear acrylic in order to provide optical access to the mini-sac and the internal holes. Figure 3 (a) and (b) shows how the original nozzle was modified and the new optically accessible acrylic nozzle fitted.

Figure 3: (a) Non-modified nozzle (b) Modified nozzle

The profile drawing of the optically accessible acrylic nozzle tip is shown in Figure 4. Drawings of the original nozzle design were provided by the diesel nozzle manufacturer. The conical face (needle seal surface), mini-sac and hemispherical base was machined manually. Six symmetric 136 µm holes were then drilled from the outside surface inwards using a CNC machine drill and customized jig. The internal dimensions of the acrylic mini-sac tip were the same as the section cut off of the real nozzle tip. The nozzle hole angle was increased from 15^{o} to 25^{o} in order to produce a clear and distinct view of each of the nozzle holes. However, only two of the nozzle holes could be viewed in focus, due to the very small depth of field achievable during imaging. These holes are identified in Figure 4 as holes 1 and 2.

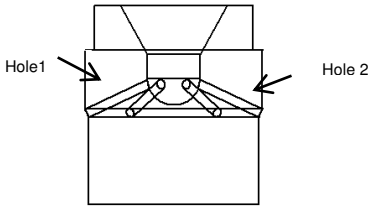

Figure 4. Nozzle interior image showing increased nozzle hole angle.

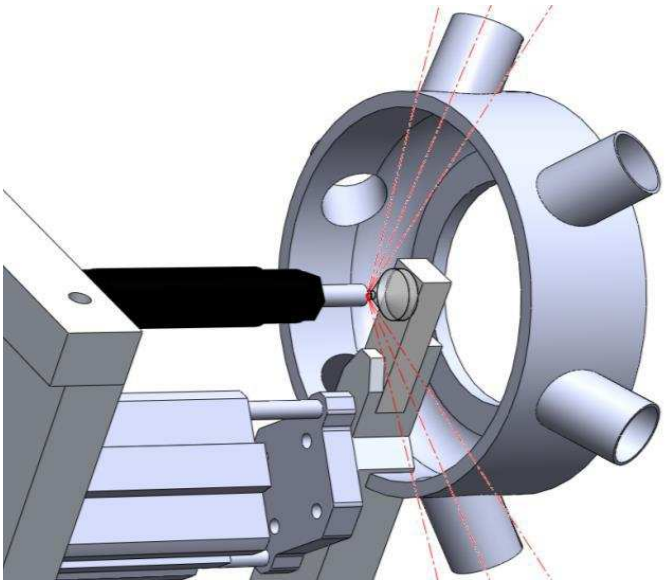

Figure 5. Isometric view of injector, mounts, and fuel spray extract assembly.

The optically accessible acrylic nozzle was required to be sealed to the base of the nozzle body during fuel injection, as shown in Figure 3 (b). A double acting pneumatic air ram attached to a balanced arm and acrylic bar, was employed to apply an axial force to a fused silica cone, which provided the axial force necessary to seal the acrylic nozzle against the flat steel nozzle base.

The components involved in mounting the injector and the optically accessible nozzle tip were not permitted to intersect the path of the spray jets emanating from the nozzle holes, and interfere with the optical access to the nozzle holes and the sac volume. The fuel spray

contained Rhodamine-B (RhB) which is a skin irritant and potential lung irritant. Therefore a fuel spray exhaust extract unit was manufactured and connected to a suction fan and filter, before being passed into the exhaust extraction system. An isometric view of the complete assembly is shown in Figure 5. The location of the acrylic bar and the 35^{o} fused silica cone are clearly observable in the figure.

Preparation of the fuels for fluorescence

The fuels employed in this study are identified by A and B. Fuel A was an unadditised crude oil derived middle distillate diesel, while Fuel B was a light kerosene. Their physical properties and boiling point range are shown in Table 1 [34].

In order to produce fluorescence, the laser light passing through the emerging spray must have a wavelength lying near the peak of the absorption spectrum of the dye to be used. Rhodamine-B (RhB) was selected to be used as the tracer dye in these experiments, due to its accessible excitation wavelength near 530 nm, fluorescence efficiency and broad-band emission wavelength range of 560 nm – 600 nm, and its relative safety.

RhB is not readily soluble in diesel fuel. Hence a suitable solvent matching the boiling profile of the fuel to be tested was selected for mixing. HPLC grade 1-Decanol and 1-Octanol supplied by Sigma-Aldrich were selected to be mixed with fuel A and fuel B respectively. Stock solutions of 0.60 g RhB in 1.0 litre volumes of 1-decanol and 1-octanol were mixed with 4.0 litres of diesel A and light kerosene B respectively, creating solutions of 0.12 g/l RhB in 1-decanol-diesel and 1-octanol-kerosene mixtures.

Table 1. Physical properties of fuels A and B.

Fuel	Physical properties			Boiling point range
	Density (kg/m^3)	Viscosity (mm^2/s,@40C)	Surface tension (mNm)	Celsius degrees (^{o}C)
Fuel A	825	2.078	31.39	170 – 350
Fuel B	800	1.664	28.46	150 – 210

The fluorescence emission yield obtained from a fluorescent dye is dependent on the solvent employed. Therefore it was necessary to determine the relative fluorescence yield from the RhB-octanol-kerosene mixture against the RhB-decanol-diesel mixture in order to make comparatively quantitative measurements of fluorescence emission intensity. In this regard, a

set of calibration measurements of relative fluorescence emission yield were undertaken for the two mixtures, which showed that the RhB-octanol-kerosene mixture produced 1.04 times the fluorescence emission yield of the RhB-decanol-diesel mixture.

The optically accessible acrylic injector nozzle was employed to measure the injected mass using unadditized diesel sample A at 350 bar common rail pressure. A rubber container of known mass was placed over the injector in order to capture the injected fuel. Four sets of 50 injections each were undertaken. The mass of the container and captured fuel was measured, facilitating the determination of the injected fuel mass.

Optical Configuration

The Laser Sheet Dropsizing (LSD) experiment required simultaneous high-speed imaging of Planar Laser Mie Scattering (PLMS) and Planar Laser Induced Fluorescence (PLIF) to be obtained from one of the diesel sprays jets emitted from the nozzle during injection. In this regard, a New Wave Research Pegasus-PIV dual head diode-pumped Nd:YLF laser operating at 527 nm, 180 ns FWHM pulse duration, 10 kHz repetition rate, 10 W continuous output power, was synchronized with the Start-of-Injection (SoI) signal, and passed through a 50 mm diameter focusing lens (1.0 m focal length), and an 8x cylindrical telescope (- 25 mm, + 200 mm cylindrical lenses) to form a laser sheet 20 mm high and 0.25 mm wide at its focus. The 20 mm high 10 kHz pulsed laser sheet was directed through the centre of the 25^{o} forward angle, vertical spray jet emitted from the nozzle, producing elastic Mie scattering (527 nm) and broad-band RhB LIF scattering at 570 nm - 590 nm.

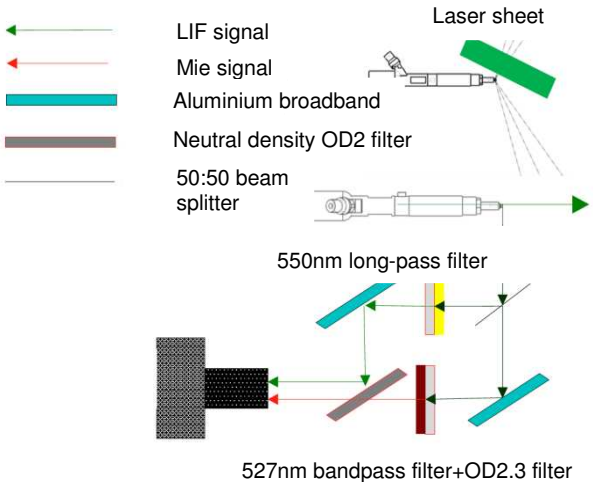

Figure 6. The LIF/Mie scattering two-channel imaging setup

The elastic (Mie) and inelastic (LIF) scattered light was imaged onto a Photron FASTCAM SA1.1 high-speed video camera synchronized to the laser at 10 kHz and the SoI signal, using a two-channel optical imaging system and an extended, inverted 85 mm, f1.4 Nikon camera lens. This configuration facilitated a 1024 x 512 pixel field-of-view with an optical magnification of 0.70, resulting in two object fields of view of 14.6 mm x 14.6 mm (corresponding to a spatial resolution of 0.028 mm/pixel), a frame exposure duration of 370 ns, and 12-bit dynamic range. The camera was set to acquire 100 frames per injection, timed to produce approximately 17 frames prior to the spray entering the field-of-view, 50 frames

during the spray and 33 frames after the spray had disappeared. The two-channel optical arrangement is shown in Figure 6.

Data Processing

External Spray Drop-sizing Distribution

Each experimental set involved the injection of one of the diesel fuel samples into air, operating at common rail pressures of 250 bar and 350 bar respectively. The camera was set to acquire 100 frames per injection event at 10 kHz for 10ms duration. Data were collected from 100 and 65 successive injections in case of fuel A and fuel B respectively; hence each experimental set consisted of 10,000 image frames for fuel A and 6,500 image frames for fuel B, per rail pressure.

The 512 x 1024 pixel image frames contain both LIF and Mie scattering data. Following the tests, a set of background images were obtained, from which a mean background image was produced. This was subtracted from all of the experimental image frames, which were then separated into two 512 x 512 pixel images of background-subtracted LIF and Mie scattering image frames.

In order to express the processing of the data images mathematically, the pixel intensities on the raw data image frames were represented by S_{ij}^{klm}, where S_{ij}^{klm} represented the intensity of the pixel located on the CCD chip at the position defined by the row index i and the column index j, $i \in \{0,1,2 \ldots,512\}$, $j \in \{0,1,2 \ldots,1024\}$. The index number k represents the frame number within a set of 100 images for a single injection event, ranging from frame 1 to frame 100; while the index number l refers to the specific injection event, ranging from injection 1 to injection 100 for fuel A and injection 1 to injection 65 for fuel B. The index number m referred to the diesel fuel sample tested, namely A or B. Figure 7 shows a single image frame of the raw, unprocessed simultaneous LIF and Mie scattering signal obtained from the diesel spray, which was captured on the high speed video camera.

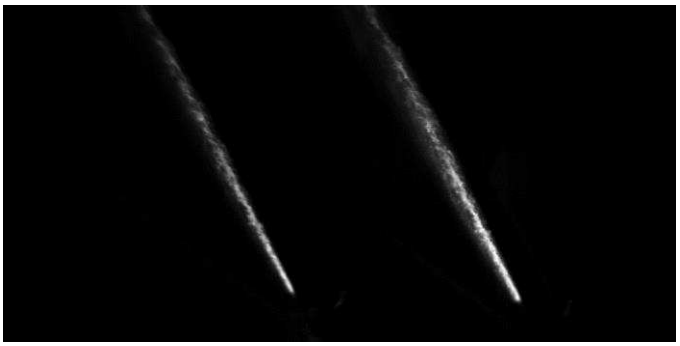

Figure 7. A combined LIF-MIE image frame captured in the LSD camera showing LIF scattering from the dye on the left and Mie scattering from the spray on the right hand side.

1000 background images were obtained for each experimental session. These pixel intensity data are represented by the indexed intensity variable B_{ij}^{mq} where the index numbers i, j and m retain their meaning from above, while the index number q refers to background image 1 to 1000. A mean background image was calculated for each experimental session. This is expressed by Equation 1.

$$\overline{B_{ij}^{m}} = \frac{1}{1000}\sum_{n=1}^{N} B_{ij}^{mq} \quad (27)$$

The mean background subtracted image is represented as I_{ij}^{klm} and is equal to $S_{ij}^{klm} - B_{ij}^{m}$. I_{ij}^{klm} is then split into two images of $i, j \epsilon \{0,1,2 \ldots, 512\}$ namely, LIF_{ij}^{klm} and Mie_{ij}^{klm} respectively. These are shown in Figure 7.

As can be observed from Figure 6 and Figure 7, the ratio cannot be obtained directly as the Mie scattering image frames are geometrically distorted relative to the LIF image frames due to the different optical paths through the beam-splitter, filters and mirrors. This required the Mie scattering image frames to be homographically aligned to that of the LIF image frames. This is an eight degree of freedom transformation, which is described by translation (2 DoF), rotation (2 DoF), shear (2 DoF) and scale (2 DoF).

An enhanced correlation coefficient (ECC) algorithm developed by Evaggelidis and Psarakis [35 – 37] was embedded in an in-house developed Matlab code to achieve the translation and homographic transformation of the images. The code allowed a template image and the image to be transformed to be input, followed by a computation of the transformation of the input image with respect to the template. It then outputted the transformed image with the corresponding transform matrix linking it to the template image. The sequence of LIF image frames LIF_{ij}^{klm} were used as the template image frames, while the Mie image frames Mie_{ij}^{klm} were the input image frames to be transformed to transformed image frames denoted by $MieHOM_{ij}^{klm}$.

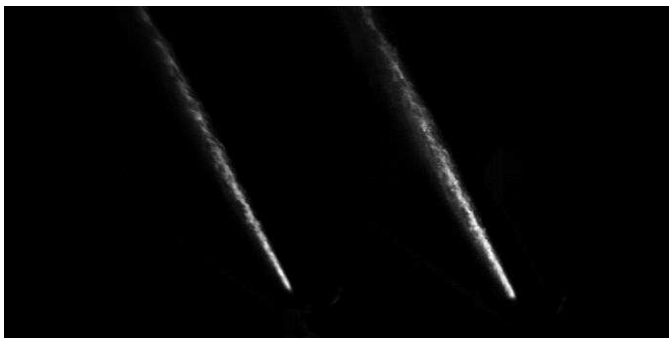

Figure 8. Split LIF (left hand side) and Mie (right hand side) images into two 512 x 512 images

The numerically calculated parameters of importance were saved for later use and an image ratio of the LIF image with the corresponding homographically corrected Mie image was also calculated to determine the instantaneous relative Sauter mean diameter (SMD) distribution of the sprays.

$$SMD_{ij}^{klm} = \frac{LIF_{ij}^{klm}}{MieHOM_{ij}^{klm}} \quad (28)$$

The SMD image frames were then converted into false color within the relative SMD range of 0 – 1.5 pixel intensity. The user defined color map is imbedded in Figure 9. The false colour map for the spray and the corresponding colour bar shown in Figure 9 are a simple ratio of the processed PLIF image to the homographically corrected planar Mie scattering image. The local signal produced by the ratio reflects the relative local volume to surface area ratio, which in the case of a diffuse spray, is the relative distribution of Sauter mean diameter. The SMD image data presented here is therefore relatively quantitative, and not absolutely quantitative. A quantitative calibration (using PDA for example) is necessary to convert the relative SMD images to absolute SMD images.

In the case of fuel B, the LSD image frames were divided by the relative fluorescence efficiency calibration factor of 1.04, in order to ensure that the SMD distributions of fuel B were correctly normalized in comparison with those of Fuel A.

The simultaneous LIF and Mie scattering images captured light emitted from the sprays 3.0 mm to 18.0 mm downstream of the diesel nozzle exit. It was considered that the primary and secondary atomization was relevant in the region 12.0 mm to 18.0 mm downstream of the nozzle exit, which was the region selected for relative SMD field analysis. The 12 mm to 18 mm range downstream of the nozzle exit corresponds to 88 nozzle diameters to 132 nozzle diameters downstream of the nozzle exit.

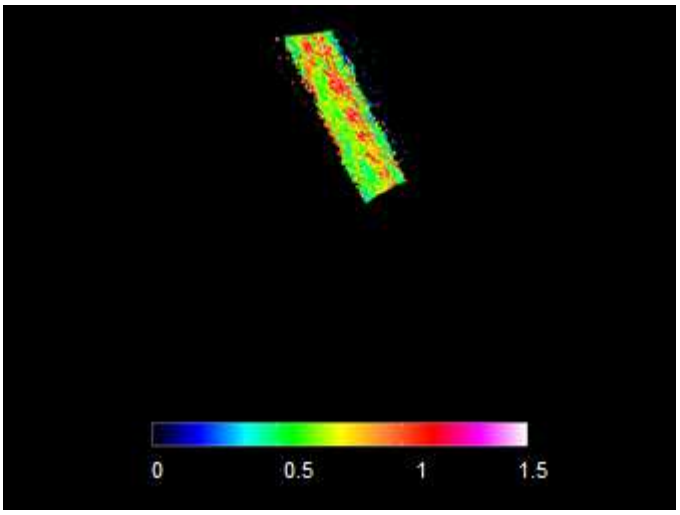

Figure 9. A false color relative SMD image of the upper 40% of the spray (12.0 mm to 18.0 mm) in the range of 0 – 1.5 pixel intensity obtained at 4.5 ms after the Start of Injection (SoI) signal began for Fuel A.

The image frames for fuel A contained low intensity secondary reflections (50 counts to 100 counts contamination signal), which had to be corrected along the edges of the spray. The image frames were filtered using a Gaussian filter, which was followed by Gaussian edge detection in order to determine the spray boundaries. One of the corrected SMD_{ij}^{klm} image frames is reproduced in false color in Figure 9.

A set of instantaneous mean SMD images were obtained from SMD_{ij}^{klm} for a set of l = 100 injections in the case of fuel A and l = 65 injections in the case of fuel B. This involved finding the mean images, to be derived from image frames 1, 101, 201,… 9901; 2, 102, 202,…, 9902 and so on up to frame 100, 200,…, 10,000 for fuel A, and similarly frames 1, 101, 201,… 6401; 2, 102, 202,…, 6402 and so on up to frame 65, 165, 265,…, 6500 for fuel B.

Frame 45 is used for the purpose of this analysis. The spray produced at this time corresponded to that associated with maximum needle lift for each injection (4.0ms after SoI). This is expressed mathematically by

$$\overline{SMD_{ij}^{45m}} = \frac{1}{No.\ of\ injections}\sum_{l=1}^{No.inj} SMD_{ij}^{45lm} \qquad (29)$$

The largest mean SMD signal for all of the spray data presented here occurred along the central axis of the 250 bar spray produced using fuel A (Figure 10). The mean of the top 1 % of pixel intensities has been normalized to provide an SMD ratio value of 1.000. The false colour mean SMD image pixel intensities shown in the Results section for all other spray cases has been normalized against the maximum value of 1.000 shown in Figure 10. Therefore all of the mean SMD image data for all cases presented are relatively comparable.

Five intensity frequency histograms of the mean SMD image acquired 4.5 ms after SoI (frame 45), were produced with 100 bins between 0.010 and 1.000 for both fuel samples and rail pressures. The histograms represent the relative droplet size distribution at five different regions of the spray. The regions under examination were: (1) spray boundaries, (2) areas between the spray boundaries and core, (3) spray core, (4) left half of spray and (5) right half of spray.

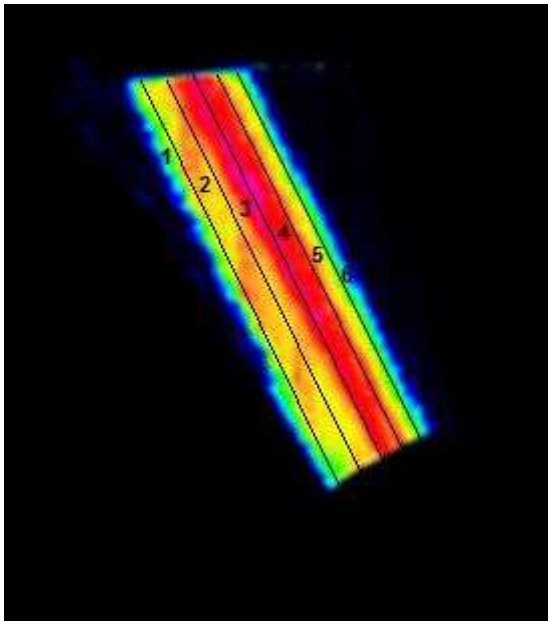

Figure 10. A false color image of SMD distribution showing the six image segments subjected to statistical analysis.

A Matlab code developed at City University facilitated the precise determination of the upper and lower extreme points of the spray. The mid-points of the upper and bottom edges were calculated, together with the determination of the spray centerline. The code then split the spray body into two approximately equal divisions, the left and right spray halves.

Each division was then divided into three equally spaced segments. Consequently, the spray was divided into six equal segments, which were paired in order to produce: (1) two SMD graphs defining the SMD distribution of droplet size in the sprays on (a) the right hand side of the spray centre-line, and (b) the left hand side of the spray centre-line, and (2) three SMD graphs defining the SMD distribution of droplet size obtained in the spray, along (a) the boundary (periphery) of the spray, (b) the centre-line segment of the spray, and (c) the segment between the boundary and the centre-line. The six segments employed for the statistical analysis are shown in Figure 10.

Results and Discussion

General Observations

Spray Core, Primary and Secondary Atomization

Figure 8 shows a single shot PLIF and Mie scattering image obtained from one of the diesel sprays formed during injection. The field of view shows the spray 3.0 mm downstream of the nozzle exit (22 nozzle diameters) to 18 mm downstream of the nozzle exit (132 nozzle diameters). The processed SMD data images presented in the Results section showed SMD data 12.0 mm (88 nozzle diameters) to 18.0 mm (132 nozzle diameters) downstream of the nozzle exit. In this region, primary atomization around the core of the spray should be coincident with secondary atomization of the spray surrounding the spray core [11].

Figure 8 reveals that Lorentz-Mie scattering provides useful qualitative detail regarding the structure of the spray. Aside from the useful measurements of spray cone angle and spray head motion, the images are unable to provide quantitative information about the spray structure. In contrast to this, Planar Laser Induced Fluorescence (PLIF) images are able to provide relatively quantitative information on local liquid volume fraction, and hence identify the location of the spray core, and where primary and secondary atomization occur.

An examination of the Mie scattering image shown in Figure 7 suggests that the spray core survives a minimum distance of 10.5 mm downstream of the nozzle exit (~ 76 nozzle diameters). An examination of the PLIF image in Figure 7 shows that the local liquid volume fraction (as indicated by LIF) begins to drop significantly at approximately 8.0 mm downstream of the nozzle exit (~ 59 nozzle diameters).

An examination of the three LIF spray images shown in Figure 11 reveals that the spray core survives a minimum distance of 10 mm (left spray, 74 nozzle diameters) to 11 mm (right spray, 81 nozzle diameters) downstream of the nozzle exit.

Spray Vorticity

Figure 11 shows three single-shot grey scale images of instantaneous laser induced fluorescence obtained from the diesel spray during injection.

The left and right hand images suggest that the spray cores contain a helical twist (blue arrows, ~ 9 mm downstream of nozzle exit) that appear to break down to form secondary helical structures (red arrows, ~ 12 mm downstream of nozzle exit), which then break down further into ligaments and/or bunched groups of droplets (combined primary and secondary atomization (14 mm – 18 mm).

Helical structures observed in the near jet would suggest that the liquid jet flow leaving the nozzle exit has angular momentum. The jet angular momentum would be expected to dissipate as the jet turbulence dissipated, the jet interacted with the surrounding air, and was atomized. This suggestion is consistent with other measurements and modelling results [6, 7], which show that that the diesel flow inside the nozzle holes has angular momentum (swirl), which often results in vortex cavitation. Simultaneous time-resolved high-speed video imaging of white light scattering from discontinuous cavitation flow surfaces in these optically accessible model injectors suggests that vortex cavitation was present in the nozzle holes for all of the fuel tests conducted [38, 39].

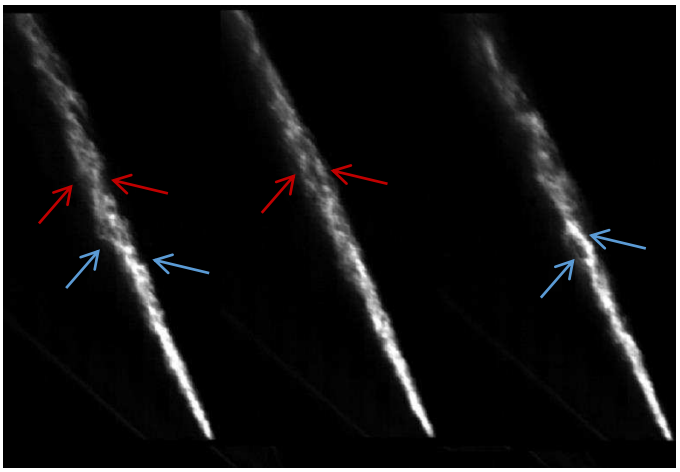

Figure 11. Structural vorticity of the sprays. The blue arrows suggest a twisted helicoid liquid core. The red arrows suggest a region of diffuse, interlinked helical spray structure. (Fuel B, 350bar, between 4.7-4.8 ms after SoI).

Laser Sheet Drop-Sizing – Fuel A

Injected Fuel Mass

The maximum and minimum injected fuel masses obtained from the optically accessible acrylic injector at 350 bar were measured to be 2.781 g and 2.802 g respectively for 50 injections. Hence the mean injected fuel mass per injection was 55.82 mg ± 0.02 mg. This corresponds to a discharge coefficient of approximately 0.660 based on a 4.0 ms injection period. Consequently the relative discharge coefficient and injected mass for the acrylic nozzle (0.660, 55.82 mg) is 20.4 % smaller than that for the conventional nozzle (0.830, 70.19 mg). It is suggested that the difference in injected mass and discharge coefficient was due to the increased surface roughness of the acrylic nozzles relative to the conventional diesel nozzle.

250 bar Results

Figure 12 shows a false colour image of the mean relative SMD distribution of the upper region of the spray (12 mm (88 nozzle diameters) to 18 mm (132 nozzle diameters) downstream of the nozzle exit) produced from fuel A at 4.5 ms after SoI (frame 45) for a rail pressure of 250 bar.

Figure 13 shows a graph of the normalized SMD frequency (probability) as a function of relative Sauter Mean Diameter (SMD) for the entire spray (solid black curve), the left hand side of the spray (dark grey curve) and the right hand side of the spray (light grey curve). The relative SMD has been normalized such that the largest droplets present in the spray have a relative SMD of 1.0.

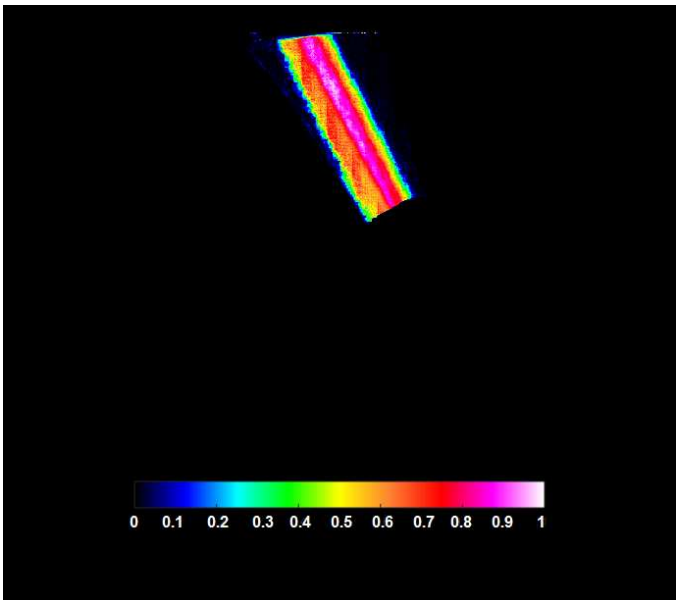

Figure 12. A false color image of SMD distribution of the 250 bar spray at 4.5 ms after SoI for Fuel A.

Figure 14 shows a graph of normalized SMD frequency as a function of relative Sauter Mean Diameter (SMD) for the equally spaced spray boundary region (periphery (solid black curve)), the region between the spray boundary and the spray centre-line (intermediate segment, dark grey curve), and the spray centre-line segment (light grey curve).

The graphs shown in Figures 13 and 14 are graphical projections of normalized histogram frequencies representative of the number of pixels in the mean spray image frame (Figure 12) with an SMD LIF/Mie ratio lying in a normalized SMD size range of 0.00 to 1.00 in discrete divisions of 0.01 (namely the fraction of droplets having a size range from 0.00 – 0.01, 0.01 – 0.02, 0.02 – 0.03, …., 0.98 – 0.99, 0.99 – 1.00). Adopting this approach means that the area under the graph is properly normalized to one, and that the normalized frequency represents the probability of finding droplets in the spray with the specified range of Sauter Mean Diameter.

As the 250 bar spray for fuel A produces the largest SMD ratio for all of the SMD data presented here, the image data is normalized such that the top 1 % of pixel intensities present in Figure 12 is normalized to an SMD ratio value of 1.000. All of the other spray image data presented here was then normalized to corresponding relative values, in order to make their SMD ratios comparable to those obtained in Figure 12.

A visual comparison of the left and right hand side of the centre-line of the spray SMD distribution in Figure 12 suggests that the 250 bar spray has developed in an asymmetric manner. This is confirmed by a comparison of the graphs for the left hand side of the spray center-line and the right hand side of the spray centre-line in Figure 13, which show quantitatively the asymmetry present in the 250 bar spray. The right hand side spray segment contains droplets with significantly larger droplets than the left hand side of the spray. The right hand side of the spray is associated with the flow occurring adjacent to the upper surface of the injector nozzle, and the left hand side of the spray is associated with the flow occurring adjacent to the lower surface of the injector nozzle. The geometry of cylindrical multi-hole mini-sac diesel injector nozzles supports the development of geometric sheet cavitation to occur at the upper entrance to the nozzle holes due to the local flow acceleration, pressure gradient and shear flow occurring as the flow enters the nozzle holes. It is suggested that the asymmetry in the spray structure and the SMD distribution downstream of the nozzle exit was caused by the flow asymmetry produced in the nozzle holes by the geometric sheet cavitation.

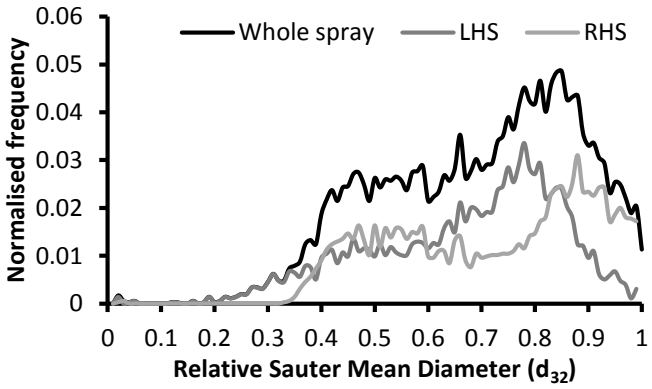

Figure 13. Graph of normalized frequency (probability) as a function of relative SMD of the whole, the left half and the right half, 250 bar spray at 4.5 ms after SoI for Fuel A.

The SMD distribution for the whole spray shown in Figure 13 has a mean and standard deviation SMD of 0.705 and 0.191 respectively. The left hand side segment of the spray centerline has a mean and standard deviation of 0.673 and 0.180 respectively, while the right hand side segment of the spray has a mean and standard deviation SMD of 0.737 and 0.196 respectively.

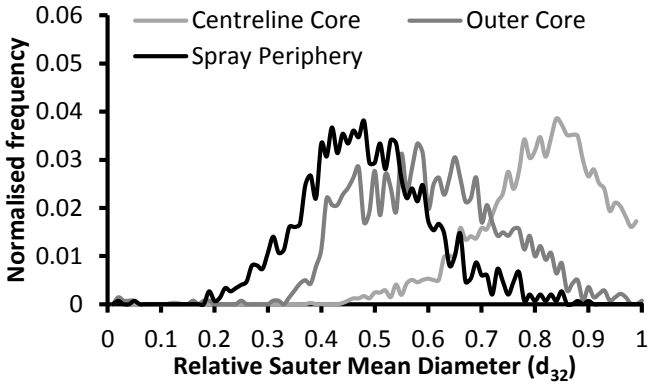

Figure 14. Graph of normalized frequency (probability) of the centre-line segment, intermediate segment and periphery segment of the 250 bar spray as a function of relative SMD at 4.5 ms after SoI for Fuel A.

A comparison of the graphs shown in Figure 14 reveal that the centerline segment of the spray contained the largest droplets (mean and standard deviation SMD of 0.820 and 0.140), followed by the droplets in the intermediate segment between the centre-line region and the periphery region (mean and standard deviation SMD of 0.598 and 0.121). Finally the smallest droplets were found in the periphery segment of the spray (mean and standard deviation SMD of 0.485 and 0.124). This is unsurprising, as this is where the secondary atomization occurred in the spray.

350 bar Results

Figure 15 shows a false colour image of the mean relative SMD distribution of the upper region of the spray (12 mm (88 nozzle diameters) to 18 mm (132 nozzle diameters) downstream of the nozzle exit), produced from fuel A at 4.5 ms after SoI (frame 45) for a rail pressure of 350 bar.

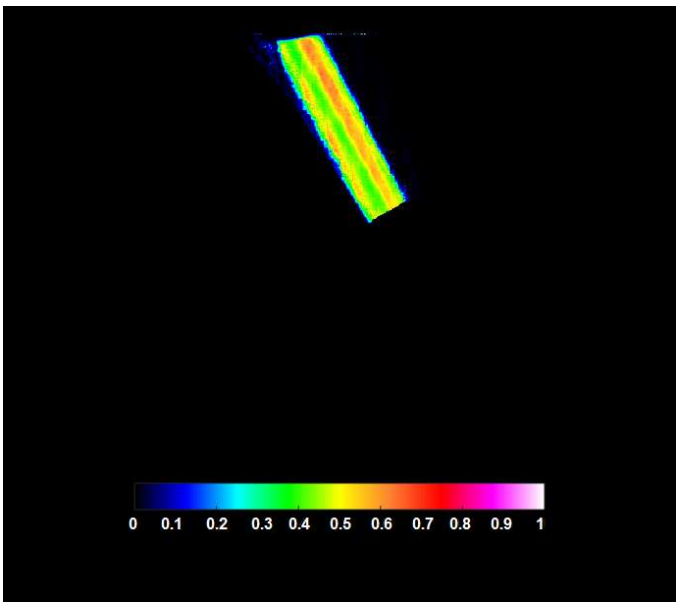

Figure 15. A false color image of SMD distribution of the 350 bar spray at 4.5 ms after SoI for Fuel A.

Figure 16 shows a graph of the normalized SMD frequency (probability) as a function of relative Sauter Mean Diameter (SMD) for the whole spray (black curve), the left hand side of the spray centerline (dark grey curve), and the right hand side of the spray centre-line (light grey curve). The relative SMD has been normalized against the top 1 % of drop sizes observable in Figure 12. Therefore the relative Sauter Mean Diameter (SMD) distributions are comparable to those shown in Figures 12 to 14.

Figure 17 shows graphs of normalized SMD frequency as a function of relative Sauter Mean Diameter (SMD) for the equally spaced spray boundary region, the region between the spray boundary and the spray centre-line, and the spray centre-line region.

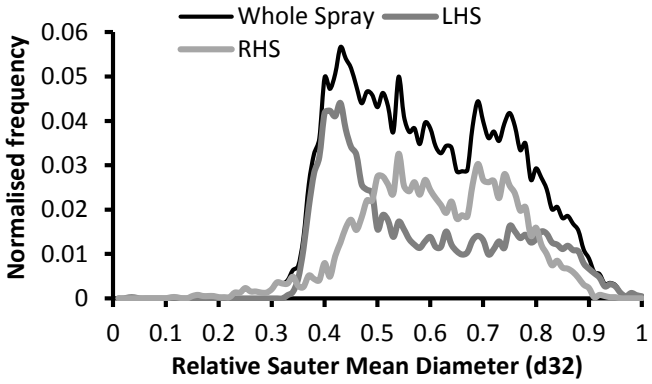

Figure 16. Graph of normalized frequency (probability) as a function of relative SMD of the whole, left hand side and right hand side of the 350 bar spray at 4.5 ms after SoI for Fuel A.

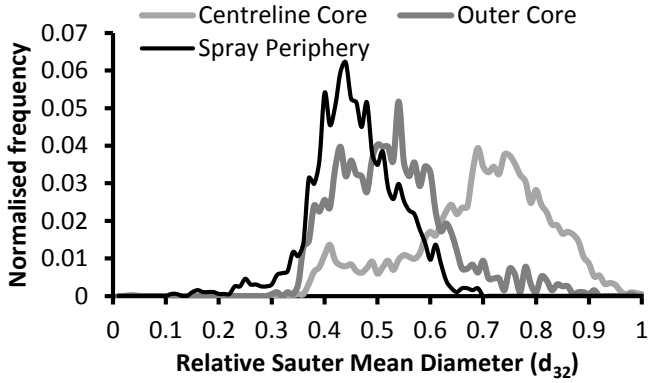

Figure 17. Graph of normalized frequency (probability) of the centre-line, intermediate and periphery segments of the 350 bar spray as a function of relative SMD at 4.5 ms after SoI for Fuel A.

A comparison of the graphs for the left hand side of the spray center-line and the right hand side of the spray centre-line in Figure 16 shows the asymmetry of the 350 bar spray. The right hand side spray segment contains droplets with significantly larger droplets than the left hand side of the spray. The SMD distribution for the whole 350 bar spray shown in Figure 16 has a

mean and standard deviation SMD of 0.594 and 0.155 respectively. The left hand side segment of the spray centerline has a mean and standard deviation of 0.575 and 0.169 respectively, while the right hand side segment of the spray has a mean and standard deviation SMD of 0.613 and 0.137 respectively.

The SMD distribution obtained from fuel A at 350 bar (Figures 15 and 16) reveal that the SMD distribution has the expected asymmetric SMD profile, but with an unusual decrease followed by an increase in SMD as a function of radius from the central axis towards the left boundary of the spray. This unusual SMD spray field profile was not observed in the diesel sprays produced from the other fuels tested. However, this unusual spray SMD distribution may have one of two explanations. (1) Vortex cavitation occurring in the nozzle hole, and extending all the way to the nozzle exit may cause this unusual SMD distribution, by establishing a central region in the spray core downstream of the nozzle exit with low relative liquid volume fraction, surrounded by a swirling liquid core. (2) the jet may have been subjected to an instability caused by hydraulic flip (possibly induced by nozzle cavitation), flipping the location of the spray core between two adjacent axial centerlines.

The overall spray SMD distributions shown in Figures 12 and 13 at 250 bar, when compared with the SMD distributions obtained in Figures 15 and 16 for 350 bar show that mean diesel spray droplet size decreased with an increase in rail pressure. The unadditized diesel (fuel A) was observed to form droplets with a mean SMD 14 % smaller at 350 bar compared to the mean SMD obtained at 250 bar (0.594 versus 0.705).

A consideration of the graphs presented in Figure 17 facilitates the same conclusion as for the 250 bar spray. The central region of the 350 bar spray contains the largest droplets (mean and standard deviation SMD of 0.691 and 0.107), followed by the intermediate region between the centre segment and the peripheral segment (mean and standard deviation SMD of 0.529 and 0.083), followed by the outer third periphery of the spray (mean and standard deviation SMD of 0.458 and 0.134).

Laser Sheet Drop-Sizing – Fuel B

250 bar Results

Figure 18 shows a false colour image of the mean relative SMD distribution of the upper region of the spray produced from fuel B at 4.5 ms after SoI (frame 45) for a rail pressure of 250 bar.

Figure 19 shows a graph of the normalized SMD frequency (probability) as a function of relative Sauter Mean Diameter (SMD) for the whole spray (black curve), the left hand side of the spray centerline (dark grey curve), and the right hand side of the spray centre-line (light grey curve). The relative SMD has been normalized against the top 1 % of drop sizes observable in Figure 12. Therefore the relative Sauter Mean Diameter (SMD) distributions are comparable to those shown in Figures 12 to 17.

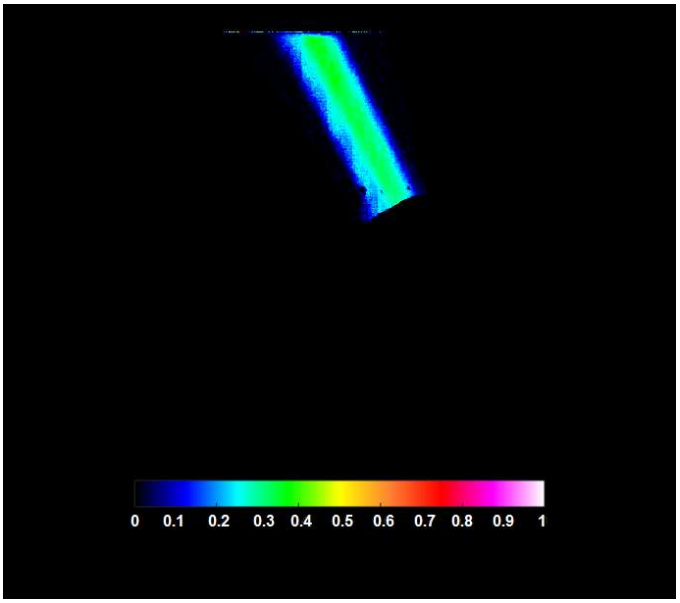

Figure 18. A false color image of SMD distribution of the 250 bar spray at 4.5 ms after SoI for Fuel B.

A visual comparison of the left and right hand side of the centre-line of the spray SMD distribution in Figure 18 suggests that the 250 bar spray for fuel B has developed in a much more symmetric manner than for fuel A. An asymmetry remains, but it is less distinctive. This is confirmed by a comparison of the graphs for the left hand side of the spray center-line and the right hand side of the spray centre-line in Figure 19, which show quantitatively the small asymmetry present in the 250 bar spray for fuel B (light kerosene). The right hand side spray segment contains droplets with slightly larger droplets than the left hand side of the spray.

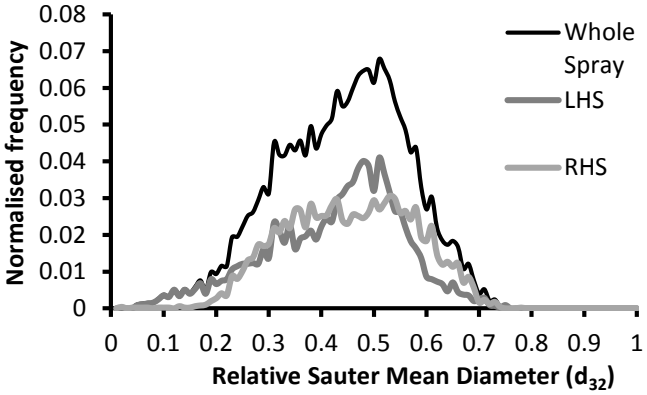

Figure 19. Graph of normalized frequency (probability) as a function of relative SMD of the whole, left hand side and right hand side of the 250 bar spray at 4.5 ms after SoI for Fuel B.

The SMD distribution for the whole spray shown in Figure 18 has a mean and standard deviation SMD of 0.441 and 0.125 respectively. The left hand side segment of the spray centerline has a mean and standard deviation of 0.427 and 0.128 respectively, while the right hand side segment of the spray has a mean and standard deviation SMD of 0.453 and 0.122 respectively.

A comparison of the mean SMD distribution produced by fuel A (unadditised diesel) with fuel B (light kerosene) reveals that fuel A forms droplets 60 % larger on average than fuel B (0.705 ± 0.191 versus 0.441 ± 0.125) at 250 bar rail pressure. This is a consequence of the difference in viscosity and surface tension between the two fuels, resulting in later primary atomization and secondary atomization in fuel A relative to fuel B.

Figure 20 shows graphs of normalized SMD frequency as a function of relative Sauter Mean Diameter (SMD) for the equally spaced spray boundary region, the region between the spray boundary and the spray centre-line, and the spray centre-line region.

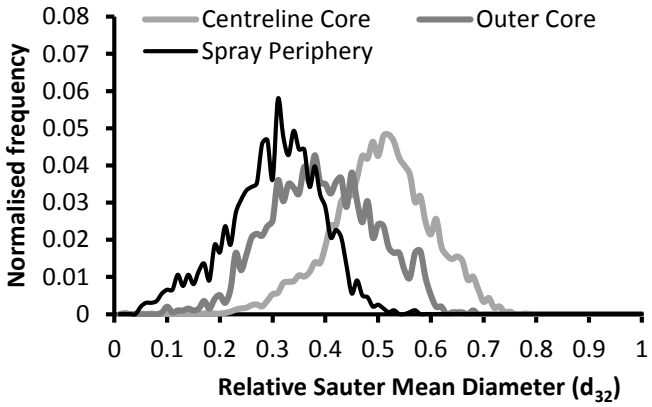

Figure 20. Graph of normalized frequency (probability) of the centre, intermediate and periphery segments of the 250 bar spray as a function of relative SMD at 4.5 ms after SoI for Fuel B.

A consideration of the graphs presented in Figure 20 facilitates a similar conclusion as for the sprays produced by fuel A. The central region of the 250 bar spray contains the largest droplets (mean and standard deviation SMD of 0.504 and 0.095), followed by the intermediate region between the centre segment and the peripheral segment (mean and standard deviation SMD of 0.395 and 0.101), followed by the outer third periphery of the spray (mean and standard deviation SMD of 0.303 and 0.088).

350 bar Results

Figure 21 shows a false colour image of the mean relative SMD distribution of the upper region of the spray for fuel B produced at 4.5 ms after SoI (frame 45) for a rail pressure of 350 bar.

Figure 22 shows a graph of the normalized SMD frequency (probability) as a function of relative Sauter Mean Diameter (SMD) for the whole spray (black curve), the left hand side of the spray centerline (dark grey curve), and the right hand side of the spray centre-line (light grey curve), obtained from fuel B (light kerosene) at 350 bar. The relative SMD has been normalized against the top 1 % of drop sizes observable in Figure 12. Therefore the relative Sauter Mean Diameter (SMD) distributions are comparable to those shown in Figures 12 to 20.

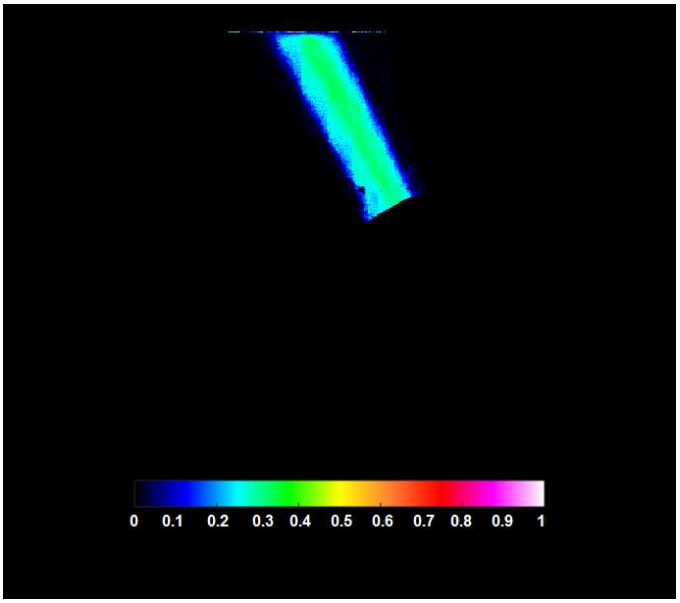

Figure 21. A false color image of SMD distribution of the 350 bar spray at 4.5 ms after SoI for Fuel B.

A visual comparison of the left and right hand side of the centre-line of the spray SMD distribution in Figure 21 suggests that the 350 bar spray for fuel B (light kerosene) exhibits a similar asymmetry to the 250 bar spray. This is confirmed by a comparison of the graphs for the left hand side of the spray center-line and the right hand side of the spray centre-line in Figure 12, which show quantitatively the small asymmetry present in the 350 bar spray for fuel B (light kerosene). The right hand side spray segment contains droplets with slightly larger droplets than the left hand side of the spray.

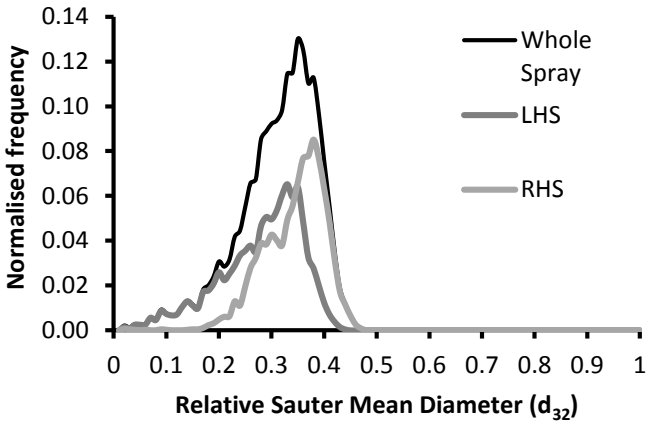

Figure 22. Graph of normalized frequency (probability) as a function of relative SMD for the whole, left hand side and right hand side of the 350 bar spray at 4.5 ms after SoI for Fuel B.

The SMD distribution for the whole spray shown in Figure 21 has a mean and standard deviation SMD of 0.318 and 0.073 respectively. The left hand side segment of the spray centerline has a mean and standard deviation of 0.280 and 0.080 respectively, while the right

hand side segment of the spray has a mean and standard deviation SMD of 0.343 and 0.060 respectively.

The overall spray SMD distributions shown in Figures 18 and 19 at 250 bar, when compared with the SMD distributions obtained in Figures 21 and 22 for 350 bar show that mean diesel spray droplet size decreased with an increase in rail pressure. The light kerosene (fuel B) was observed to form droplets with a mean SMD 27 % smaller at 350 bar compared to the mean SMD obtained at 250 bar (0.318 versus 0.441).

Figure 23 show graphs of normalized SMD frequency as a function of relative Sauter Mean Diameter (SMD) for the equally spaced spray boundary region, the region between the spray boundary and the spray centre-line, and the spray centre-line region.

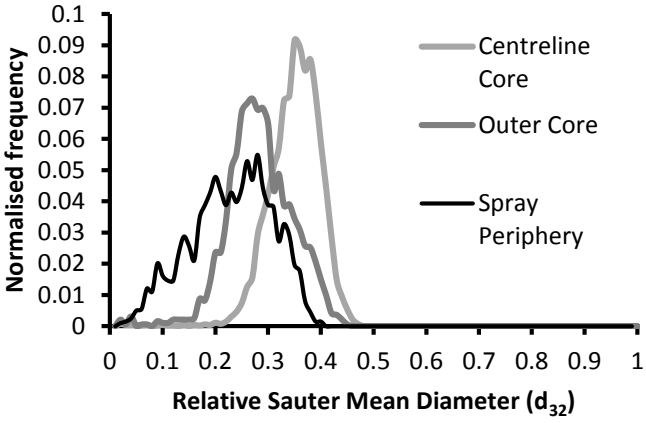

Figure 23. Graph of normalized frequency (probability) of the left hand half of the spray as a function of relative SMD of the 350 bar spray at 4.5 ms after SoI for Fuel B.

A consideration of the graphs presented in Figure 23 facilitates a similar conclusion as for all of the other sprays considered. The central region of the 350 bar spray contains the largest droplets (mean and standard deviation SMD of 0.350 and 0.049), followed by the intermediate region between the centre segment and the peripheral segment (mean and standard deviation SMD of 0.284 and 0.062), followed by the outer third periphery of the spray (mean and standard deviation SMD of 0.229 and 0.079).

A comparison of the mean SMD distribution produced by fuel A (unadditised diesel) with fuel B (light kerosene) reveals that fuel A forms droplets on average 87 % larger than fuel B (0.594 ± 0.155 versus 0.318 ± 0.073) at 350 bar rail pressure. This is a consequence of the difference in viscosity and surface tension between the two fuels, resulting in later primary atomization and secondary atomization in fuel A relative to fuel B.

The results obtained in the study have produced relative SMD distributions for diesel sprays produced from unadditized diesel and light kerosene at 250 bar and 350 bar rail pressure. In order to convert these distributions from relative SMD distributions to absolutely quantitative SMD measurements, a simultaneous Phase Doppler calibration is necessary. This is planned for future work.

Summary and Conclusion

A number of conclusions may be drawn from this work. These are summarized below:

1. Laser Induced Fluorescence is a reliable technique for the determination of regions of primary and secondary atomization in sprays, through the quantitative measurement of local liquid volume fraction.

2. The SMD droplet size distributions produced by the diesel sprays were observed to be asymmetric along the spray jet. This is judged to be a consequence of the flow asymmetry introduced into the nozzle holes as a result of geometric cavitation developing at the entrances to the nozzle holes.

3. The SMD droplet size distributions produced by these diesel sprays showed larger droplets forming towards the centre of the spray, decreasing with increasing radius from the center-line of the spray jets.

4. The mean SMD droplet sizes were observed to decrease with increasing rail pressure for both fuels A and B.

5. The mean droplet size obtained in the spray produced by Fuel B was significantly smaller than the mean droplet size obtained in the spray produced by Fuel A for both test rail pressures. This is a consequence of fuel B having lower surface tension and viscosity than fuel A.

The relatively quantitative measurements of mean and standard deviation of Sauter Mean Diameter distributions obtained in these non-evaporating sprays as a function of fuel properties and common rail injection pressure may be useful for the calibration of or comparison with theoretical and/or computational predictions for these sprays.

Finally, the images of the spray jets exiting the injector nozzles suggested the development of twisted helical structures in the liquid core, followed by the suggested formation of secondary helical spray structures further along the spray. The suggested formation of helical structures in the spray core suggests that the jets exiting the nozzle holes retained angular momentum originally developed in the injector nozzle holes.

References

1. Ikegani M. Kamimoto T, Ch. 6 - Conventional Diesel Combustion, in Flow and Combustion in Reciprocating Engines, (Editors) Arcoumanis C., Kamimoto T., Springer-Verlag Berlin Heidelberg, 2009. ISBN 978-3-540-64142-1.
2. Dec J., "A Conceptual Model of DI Diesel Combustion based on Laser-Sheet Imaging", SAE Technical Paper 970873, SAE Transactions – Journal of Engines V106-3, 1997. DOI: 10.4271/970873.
3. Heywood, J. Ch. 10 – Combustion in Compression-Ignition Engines, in Internal Combustion Engine Fundamentals, McGraw-Hill Book Company 1988. ISBN 0-07-100499-8.
4. Badock C., Wirth R., Fath A., and Leipertz A., "Investigation of cavitation in real size diesel injection nozzles", Int. J. of Heat and Fluid Flow, pp. 538–544, 1999.

5. Arcoumanis C., Gavaises M., Flora H., Roth H., "Visualisation of cavitation in diesel engine injectors", Mecanique & Industries V2:5, pp 375 – 381, 2001.
6. Arcoumanis C., Flora, H, Gavaises M., Badami, M., "Cavitation in Real-Size Multi-Hole Diesel Injector Nozzles" SAE Technical Paper 2000-01-1249, SAE 2000 Transactions Journal of Engines – V109-3 1999. DOI: 10.4271/2000-01-1249.
7. Andriotis A., Gavaises M., Arcoumanis C., "Vortex flow and cavitation in diesel injector nozzles", J. Fluid Mech 610, pp. 195 - 215, 2008.
8. Lockett R.D , Liverani L., Thaker D., Jeshani M., Tait N.P., "The characterization of diesel nozzle flow using high speed imaging of elastic light scattering", Fuel 106, 605 – 616, 2013.
9. Lefebvre A. H., Ch. 2 – Basic processes in Atomization, in Atomization and Sprays, Taylor and Francis, 1989. ISBN 0-89116-603-3.
10. Guildenbecher D.R., Lopez-Rivera C., Sojka P.E., "Secondary Atomization", Exp. Fluids v46:3, pp371 – 402, 2009.
11. Faeth G.M., Hsiang, L.-P., Wu, P.-K., "Structure and Breakup Properties of Sprays", Int. J. Multiphase Flow v21, pp99 – 127, 1995.
12. Lin S.P., Reitz R.D., "Drop and Spray Formation from a Liquid Jet", Annu. Rev. Fluid. Mech. v30, pp85 – 105, 1998.
13. Wu P.-K., Miranda R.F., Faeth G.M. "Effects of initial flow conditions on primary breakup of nonturbulent and turbulent round liquid jets", Atom. Sprays v5, pp175 – 196, 1995.
14. Wu P.-K., Faeth G.M., "Aerodynamic effects on primary breakup of turbulent liquids", Atom. Sprays v3, pp265 – 289, 1993.
15. Cheroudi B., Onuma Y., Chen S.-H., Bracco, F.V., "On the intact core of full-cone sprays", SAE Tranactions v94-85: Paper 850126, 1985.
16. Hsiang L.-P., Faeth G.M., "Near limit dop deformation and secondary breakup", Int.J.Multiphase Flow v19, pp721 – 735, 1992.
17. Ghurri A., Kim J.-D., Kim H. G., Jung J.-Y., and Song K.-K., "The effect of injection pressure and fuel viscosity on the spray characteristics of biodiesel blends injected into an atmospheric chamber", Journal of Mechanical Science and Technology, pp. 2941–2947, 2012.
18. Jankowski A., Siemińska-Jankowska B., Sandel A., and Bocheński C., "Investigation of the fuel spray atomization spectrum in common-rail system for diesel engines", Journal of KONES, pp. 53–64, 2003.
19. Chen P-C, Wang W-C, Roberts L.R,b, Fang T., "Spray and atomization of diesel fuel and its alternatives from a single-hole injector using a common rail fuel injection system'', Fuel, Vol.103, pp.850-861, 2013.
20. Durst F., Brenn G., Xu T.H., "A review of the development and characteristics of planar phase-Doppler anemometry", Meas.Sc.Tech. v8:11, pp1203 – 1221, 1997.
21. Black D.L., McQuay M.Q., Bonin M.P., "laser-based Techniques for Particle Size Measurement: A Review of Sizing Methods and Their Industrial Applications", Prog. Energy Combust. Sc. V22, pp267 – 306, 1996.
22. Greenhalgh D.A., "Laser imaging of fuel injection systems and combustors", Proc. Inst. Mech. Eng 214.4, pp367 – 376, 2000.
23. Yeh C.Y., Kosaka H., Kamimoto T., "Measurement of Drop Sizes in Unsteady Dense Sprays", Ch. 12, Recent Advances in Spray Combustion: Spray Atomization and Drop Burning Phenomena Volume 1, Ed. K. Kuo, Vol. 166, Pro. Astro. Aero., 1996.
24. Le Gal P., Farrugia, N., Greenhalgh D., "Laser Sheet Dropsizing of Dense Sprays", Optics and Laser Technology v31:1, pp 75 – 83, 1999.
25. Jermy M.C., Greenhalgh D.A., "Planar dropsizing by elastic and fluorescence scattering in sprays too dense for phase Doppler measurement", Appl. Phys. B 71, pp703 – 710, 2000.

26. Berrocal E., Kristensson E., Richter M., Linne M., Alden M., "Application of structured illumination for multiple scattering suppression in planar laser imaging of dense sprays", Optics Express v16:22, pp 17870 – 17881, 2008.
27. Linne M. Paciaroni, Hall T., Parker T., "Ballistic imaging of the near field in a dense spray", Exp. Fluids v40 pp836 – 846, 2000.
28. Powell, C.F., Duke D., Kastengren A.L., Ilavsky J., "Measurements of Diesel Spray Droplet Size with Ultra-Small Angle X-Ray Scattering", 25th Ann. Conf. Liq. Atom. Spray Systems, 2013.
29. Lockett R.D., Greenhalgh D. Richter J. "The Characterization of a Diesel Spray using Combined Laser Induced Fluorescence and Laser Sheet Dropsizing", CLEO-EQEC, 1998. DOI: 10.1109/CLEOE.1998.719142.
30. Lockett R.D. and Greenhalgh D., "The Optical Characterization of Spray and Soot Formation in a Diesel Engine", Paper o84, Proceedings of the International Conference on *Sustainable Combustion (SPEIC'10)*, Canary Islands, 2010. DOI: 10.13140/2.1.1166.4324.
31. Domann R., Hardalupas Y., "Spatial distribution of fluorescence intensity within large droplets and its dependence on dye concentration", Applied Optics v 40:2, pp 3586 – 3597, 2001.
32. Van de Hulst H.C. Light Scattering by Small Particles, Dover Publications Inc, 1957, reprinted 1981. ISBN-10 0-486-64228-3.
33. Grandy W.T., Scattering of Waves from Large Spheres, Cambridge University Press, 2000. ISBN 0-521-02124-3.
34. Price R. Shell Global Solutions, Private Communication, 2013.
35. Evangelidis G. D., and Psarakis E. Z., "Projective Image Alignment by Using ECC Maximization.," VISAPP (1), pp. 413–420, 2008.
36. Evangelidis G. D., and Psarakis E. Z., "Parametric image alignment using enhanced correlation coefficient maximization," Pattern Analysis and Machine Intelligence, IEEE Transactions on, pp. 1858–1865, 2008.
37. "ECC Image Alignment Algorithm," ECC Image Alignment Algorithm[Online]. Available: http://xanthippi.ceid.upatras.gr/people/evangelidis/ecc/.
38. Jeshani M. "Optical Characterization of Cavitating Flows in Diesel Fuel Injection Equipment", PhD Thesis, City University, London, 2014.
39. Lockett R.D., Jeshani M., Price R., to be published, 2016.

Contact Information

Corresponding Author: R.D. Lockett

Email: r.d.lockett@city.ac.uk

Acknowledgments

The authors would like to acknowledge Shell Global Solutions, who provided the financial support for this work, and Mr G. Clow and Mr J.Ford of City University for their technical support.